

Prediction of the atomistic Hubbard U interaction from moiré system STM-images using image recognition

Nachiket Tanksale¹ and Tobias Stauber²

¹ *Universidad Internacional Menéndez Pelayo, E-28040 Madrid, Spain*

² *Instituto de Ciencia de Materiales de Madrid, CSIC, E-28049 Madrid, Spain*

(Dated: February 24, 2026)

The atomistic Hubbard interaction U , representing the on-site Coulomb repulsion, serves as a pivotal parameter in theoretical models describing of correlated systems, yet its precise experimental determination especially in moiré systems remains challenging. Scanning Tunneling Microscopy (STM) provides real-space images of the local density of states (LDOS), offering rich data sets that reflect the unique electronic structure of the material. Here, we introduce a systematic methodology for extracting the Hubbard U parameter directly from these LDOS images through the application of machine learning (ML) in the case of twisted bilayer graphene in the flat-band regime. The regression of U is highly accurate even though the image-similarity is greater than 99.98%. Subsequent data-analysis further suggest a weak crossover between the weak and strong coupling regime at $U_c/t \approx 1$.

I. INTRODUCTION

The discovery of correlated insulating states and superconductivity in twisted bilayer graphene (TBG) has had a tremendous impact on the condensed matter community, revealing a phase diagram that closely resembles that of high- T_c cuprate superconductors, including a strange-metal regime with linear-in-temperature resistivity near the superconducting dome.^{1–12} These phenomena are rooted in the emergence of nearly flat bands at magic twist angles, where structural complexity in moiré superlattices replaces chemical complexity as the main route to strong electronic correlations.^{13–22}

During the last eight years, flat-band engineering has become a central theme in van der Waals heterostructures, as many two-dimensional crystals with low-energy excitations near high-symmetry points such as K, X, or M-point²³ can be tuned into correlated regimes by twisting, often summarized by the phrase “moiré is more.”^{17–22} In TBG and related systems, strong Coulomb interactions drive cascade-like phase transitions at integer fillings, interaction-induced reconstruction of the band structure, and flavor (spin and valley) symmetry breaking, often accompanied by ferromagnetism at fractional band fillings.^{2–7,19,21} At the same time, superconductivity appears extremely sensitive to screening and sample conditions, and both electron-phonon and purely electronic pairing mechanisms have been proposed.^{12,20,24–27}

Scanning tunneling microscopy (STM) and spectroscopy play a key role in disentangling these intertwined phases, as they provide direct, real-space access to the local density of states (LDOS) and correlated gaps in moiré systems at the atomic scale.^{2–5,28,29} Recent STM experiments on magic-angle TBG have revealed Kekulé charge-density-wave order and shown that the STM signal, together with Chern-number information, can uniquely identify distinct correlated ground states.^{28,30,31} STM has thus proven to be an important technique to analyze moiré systems.^{32–37} However, de-

spite this wealth of spatially resolved data, quantitatively extracting microscopic interaction parameters, e.g., the effective on-site Hubbard repulsion U directly from FT-LDOS images remains a major open challenge and might open new opportunities also in view of the possibility to engineer magnetic phases in moiré systems.

Here, we want to test if one could in principle obtain the value of the Hubbard interaction directly from experiments by fitting our model to the LDOS. To do this, we will use machine learning (ML) which has emerged as a powerful tool to tackle inverse problems in quantum many-body physics, where one aims to infer the underlying Hamiltonian or order parameters from measured observables.^{38–41} Image-based techniques, especially convolutional neural networks (CNNs), have proven particularly effective for analyzing data-rich probes such as STM and photoemission, enabling automated detection of complex patterns and phase classification.^{42–48} Moiré systems are especially well suited for such approaches, since their enlarged unit cells expose intra unit-cell physics, while their tunability allows high-dimensional datasets to be generated from a single sample.^{45–48}

Here, twisted bilayer graphene under hydrostatic pressure is modeled within a tight-binding description supplemented by a long-range Coulomb interaction and an on-site Hubbard term, and solved self-consistently at the Hartree-Fock level.^{49–54} From the resulting eigenstates, we compute STM-accessible LDOS patterns and their Fourier transforms (FT-LDOS), which serve as “simulated STM-images” in momentum space for different values of U in the flat-band regime. A deep CNN (both a custom architecture and a ResNet-18 variant) is then trained to regress the Hubbard U directly from these FT-LDOS “STM” images, and interpretability tools (Grad-CAM and guided backpropagation) are used to identify the k -space features.^{55–57}

The paper is organized as follows. First, we introduce the tight-binding model and show how the FT-LDOS images are generated. Then, the training of the CNN is outlined. Last, we analyze the results with interpretability tools. We close with summary and outlook.

II. TIGHT-BINDING MODEL

We model twisted bilayer graphene under hydrostatic pressure realizing a magic-angle-like condition at $\theta = 3.5^\circ$, whose band structure closely resembles that at $\theta = 1.16^\circ$ without pressure.⁴⁹ The non-interacting tight-binding Hamiltonian reads

$$H_0 = - \sum_{n,m} \sum_{i,j} \sum_{\sigma} t_{n,m}^{i,j} \psi_{n,i,\sigma}^\dagger \psi_{m,j,\sigma}, \quad (1)$$

where $\psi_{n,i,\sigma}^{(\dagger)}$ are fermionic annihilation(creation) operators and the hopping parameters $t_{n,m}^{i,j} = t(|\mathbf{R}_n - \mathbf{R}_m + \mathbf{r}_i - \mathbf{r}_j|)$ only depend on the distance between lattice sites, with \mathbf{R}_n the lattice vector of unit cell n and \mathbf{r}_i the position of site i within the unit cell.⁵¹

We employ the Slater-Koster parametrization

$$t(\mathbf{r}) = V_{pp\pi} e^{\frac{a_0 - r}{r_0}} \left(1 - \left(\frac{\mathbf{r} \cdot \mathbf{e}_z}{r} \right)^2 \right) + V_{pp\sigma} e^{\frac{a_0 - r}{r_0}} \left(\frac{\mathbf{r} \cdot \mathbf{e}_z}{r} \right)^2, \quad (2)$$

with carbon-carbon distance $a_0 = 1.42 \text{ \AA}$, decay length $r_0 = 0.319 a_0$, equilibrium interlayer distance $d_\perp^0 = 3.34 \text{ \AA}$, and parameters $V_{pp\pi} = 2.7 \text{ eV}$, $V_{pp\sigma} = -0.48 \text{ eV}$.⁵¹ The compressed interlayer distance is $d_\perp = d_\perp^0 / 1.134$ for $\theta = 3.48^\circ$.⁴⁹

The full Hamiltonian is $H = H_0 + H_{\text{int}}$ with interaction $H_{\text{int}} = H_V + H_U$ comprising long-range Coulomb (H_V) and on-site Hubbard (H_U) terms given by

$$H_V = \frac{1}{2} \sum_{n,m} \sum_{i,j} \sum_{\sigma,\sigma'} V_{n,m}^{i,j} \psi_{n,i,\sigma}^\dagger \psi_{m,j,\sigma'}^\dagger \psi_{m,j,\sigma'} \psi_{n,i,\sigma}, \quad (3)$$

$$H_U = \frac{U}{2} \sum_{n,i} \sum_{\sigma} \psi_{n,i,\sigma}^\dagger \psi_{n,i,\bar{\sigma}}^\dagger \psi_{n,i,\bar{\sigma}} \psi_{n,i,\sigma}. \quad (4)$$

The Coulomb matrix elements are $V_{n,m}^{i,j} = v(|\mathbf{R}_n - \mathbf{R}_m + \mathbf{r}_i - \mathbf{r}_j|)$, implemented via the double-gated potential⁵²

$$v(|\mathbf{r}|) = \frac{e^2}{4\pi\epsilon_0\epsilon} \sum_n \frac{(-1)^n}{|\mathbf{r} + n\xi\mathbf{z}|} \xrightarrow{r \gg \xi} \frac{e^2}{4\pi\epsilon_0\epsilon} \frac{2\sqrt{2}e^{-\pi r/\xi}}{\xi\sqrt{r/\xi}}. \quad (5)$$

In the following, we will fix the screening length $\xi = 10 \text{ nm}$ and the dielectric constant $\epsilon = 10$. The on-site Hubbard interaction U can be thought of as a regularization of the Coulomb interaction at $\mathbf{r} = 0$ and shall be varied from 0 to 6 eV.^{53,54}

A. Hartree-Fock Solution

We solve the interacting system within the restricted Hartree-Fock approximation, considering only spin-symmetric solutions using the FORGE-package.^{49,58,59} The one-particle density matrix is thus restricted to solutions preserving all spatial, valley, and time-reversal

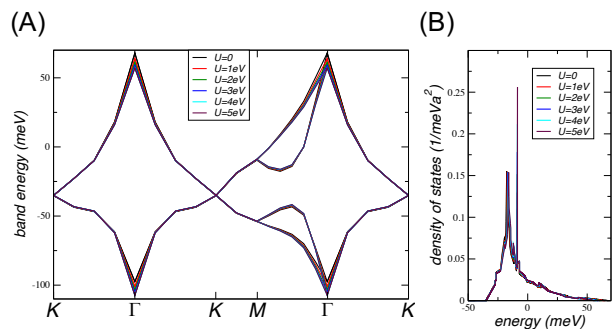


FIG. 1: (A) Hartree-Fock bands at filling $\nu = 3$ setting the Fermi energy ϵ_F to zero with $\epsilon = 10$ obeying all symmetries, for $U = 0-5 \text{ eV}$. (B) Density of states of the upper two flat bands for the same parameters.

symmetries to simplify neural-network training and we suppress the spin index σ from now on.^{20,27} In order to deal with a metallic state, we further choose an integer filling factor $\nu = 3$ and set the Fermi energy ϵ_F to zero.

Even though the atomistic Hubbard interaction is mainly associated to spin-related phenomena, there is a weak dependence on the band structure due to the localization of the wave-function around the AA-stacked region of the moiré unit cell.⁶⁰ This is shown in Figure 1(a) where the self-consistent Hartree-Fock band structure is plotted for $U = 0-5 \text{ eV}$. Only around the Γ -point, a slight variation can be seen. Consequently, the corresponding density of states of the upper two flat bands, defined by

$$\rho_\nu(\epsilon) = \frac{\mathcal{N}}{A} \sum_{\mathbf{k},n} \delta(\epsilon - \epsilon_{\mathbf{k},n}^\nu), \quad (6)$$

with A the sample area, exhibits a similarly weak U -dependence [Fig. 1(b)]. Above, we also introduced the normalization $\mathcal{N} = \sqrt{3} \sin(\theta/2)/2$ ensuring $\int a^2 \rho(\epsilon) d\epsilon$ counts bands within the energy window.

B. Local Density of States

The local density of states (LDOS) is directly proportional to the differential conductance measured by STM and therefore provides the natural bridge between our Hartree-Fock description and experimental images.²⁸⁻³⁰ It is defined as

$$\rho_\nu(\mathbf{r}_i, \epsilon) = \mathcal{N} \sum_{\mathbf{k},n} |\psi_{\mathbf{k},n}^\nu(\mathbf{r}_i)|^2 \delta(\epsilon - \epsilon_{\mathbf{k},n}^\nu), \quad (7)$$

where $\psi_{\mathbf{k},n}^\nu(\mathbf{r}_i)$ denotes the Hartree-Fock wave function at lattice site \mathbf{r}_i with quantum numbers (\mathbf{k}, n) for filling factor ν .

Instead of working directly with $\rho_\nu(\mathbf{r}_i, \epsilon)$ in real space,

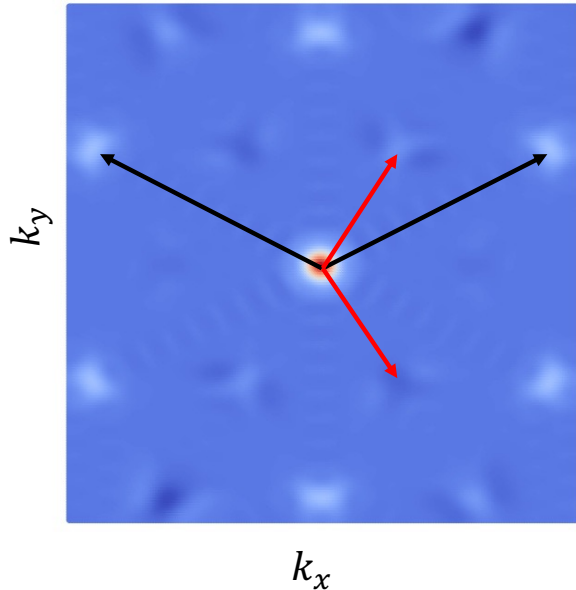


FIG. 2: Fourier-transformed LDOS (FT-LDOS) for $\nu = -2$ and $\epsilon = 12$ in the valley-coherence symmetry broken state, as discussed in Ref. 49. The principal Bragg peaks (black arrows) are located at the reciprocal lattice vectors of the two rotated graphene layers, while the red arrows indicate the reciprocal vectors associated with the Kekulé superlattice composed of three graphene unit cells.

we consider its discrete Fourier transform,

$$\rho_\nu(\mathbf{k}, \epsilon) = \sum_{\mathbf{r}_i} \rho_\nu(\mathbf{r}_i, \epsilon) e^{i\mathbf{k} \cdot \mathbf{r}_i}, \quad (8)$$

which corresponds to the momentum-space representation of STM conductance maps (FT-LDOS). In a typical \mathbf{k} -space window, the FT-LDOS is characterized by six principal Bragg peaks defined by the two reciprocal lattice vectors $\mathbf{b}_{1/2} = \frac{4\pi}{3a}(\pm 3/2, \sqrt{3}/2)$, indicated by the black arrows in Fig. 2. More precisely, the six peaks arise from the superposition of the reciprocal lattice vectors of the two rotated graphene layers.

In symmetry-broken states with valley coherence and Kekulé order, additional Bragg peaks at $\mathbf{b}_{1/2}^K = \frac{4\pi}{3a}(1/2, \pm\sqrt{3}/2)$ appear, reflecting the enlarged real-space unit cell.^{28,31,49,61} This is indicated by the red arrows in Fig. 2, where the FT-LDOS of a valley-coherence symmetry broken state at $\nu = -2$ and $\epsilon = 12$ is shown.⁴⁹ Even though we focus our training on states preserving the full spatial and valley symmetry to simplify the ML task, the intensity and evolution of these Kekulé-related peaks in nearby parameter regimes may be crucial for understanding which FT-LDOS features are picked up by the convolutional neural networks.^{47,48}

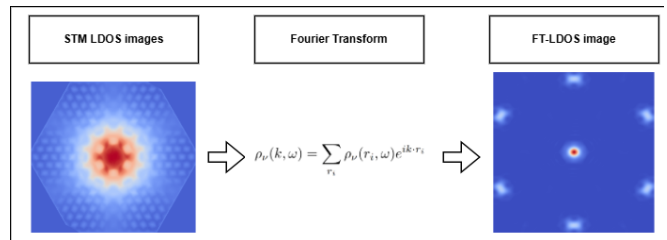


FIG. 3: Local density of states (LDOS) for $\nu = 3$ and $\epsilon = 10$ and its Fourier transformed local density of states (FT-LDOS).

III. METHODOLOGY FOR IMAGE-RECOGNITION OF FT-LDOS DATA

This section describes the generation of the theoretical dataset, the preprocessing of the Fourier-transformed local density of states (FT-LDOS), and the machine-learning architectures used to infer the interaction strength from simulated STM data.

A. Dataset Generation from Hartree–Fock Theory

We consider twisted bilayer graphene under hydrostatic pressure tuned such that a magic-angle-like flat-band regime is realized at $\theta \simeq 3.5^\circ$, with an effective band structure similar to that at $\theta \approx 1.16^\circ$ without pressure.⁴⁹ The moiré unit cell in this regime contains 1084 atoms (542 per layer), enabling self-consistent Hartree–Fock calculations including all bands and realistic long-ranged Coulomb interactions at high speed using the FORGE package.⁵⁹

For each value of the on-site Hubbard interaction U in the range 0–6 eV, we compute eigenvalues and eigenstates at integer filling factor $\nu = 3$ for fixed dielectric screening $\epsilon = 10$.⁴⁹ We restrict ourselves to spin-symmetric solutions that preserve all spatial, valley, and time-reversal symmetries, avoiding additional symmetry breaking that would require separate neural-network training. From these solutions, we generate STM LDOS maps and their FT-LDOS images at $\epsilon = \epsilon_F$, which serve as the input to the machine-learning models. This is illustrated in Fig. 3. To facilitate regression of the interaction strength, the training dataset is constructed using discrete anchor values of $U = 0, 1, 2, 3, 4$, and 5 eV, yielding a total of 600. An additional holdout dataset of 66 samples at fractional values of U is generated to assess interpolation performance. This anchor-point strategy allows the models to learn the smooth evolution of FT-LDOS features across the interaction-strength manifold while providing an independent test of generalization within the trained parameter range.

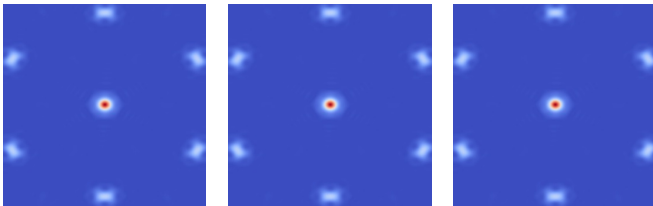


FIG. 4: Fourier-transformed LDOS (FT-LDOS) for $\nu = 3$ and $\epsilon = 10$ in the symmetric state for three random values of the Hubbard interaction $U = 0.59711$, $U = 1.56952$, and $U = 3.08776$. No difference is seen by the bare eye which is also confirmed by cosine similarity, shown in Fig. 5.

B. FT-LDOS Preprocessing

The real-space LDOS maps are Fourier transformed to obtain $\rho_{\nu=3}(\mathbf{k}, \epsilon = \epsilon_F)$, emphasizing reciprocal lattice vectors and interaction-sensitive momentum-space features commonly analyzed in STM experiments.^{28,30} The raw FT-LDOS images exhibit a dominant central moiré peak at $\mathbf{k} = 0$ as well as pronounced Bragg peaks associated with the reciprocal lattice of the two (top and bottom) graphene lattices, see Fig.4.

To ensure numerical stability and efficient training while preserving physical content, each FT-LDOS image is rescaled to a resolution of 256×256 pixels and converted to grayscale, following standard practices in image-based learning of physical systems^{42,43}. The pixel intensities are then standardized to zero mean and unit variance using statistics computed exclusively on the training set, with the same transformation applied to the test and holdout datasets. This procedure prevents information leakage between training and evaluation sets and ensures consistent normalization across samples⁶².

The full dataset is randomly partitioned into training and test subsets using an 80/20 split. Training and test splits were stratified with respect to the interaction parameter U so that each discrete U value is proportionally represented in both sets. Although stratification is not strictly required for regression tasks with continuous targets, it is appropriate here due to the discrete sampling of U in the generated dataset.

To assess robustness against sampling fluctuations, three independent splits with different random seeds are employed, and performance metrics are averaged where appropriate^{38,39}.

C. Neural-Network Architectures and Training Procedure

The inference task is formulated as a scalar regression problem, in which the goal is to predict the continuous interaction strength U from a single FT-LDOS image. We employ two convolutional neural network (CNN) architectures to balance interpretability and representational

power.

The first model is a custom-designed CNN consisting of four convolutional blocks, each comprising a two-dimensional convolution, batch normalization, and max pooling. All convolutions use 3×3 kernels with unit stride and zero padding, followed by rectified linear unit (ReLU) activations. The convolutional layers are followed by fully connected layers that map the extracted features to a single scalar output corresponding to the predicted interaction strength. This lightweight architecture is designed to preserve lattice symmetries in momentum space and to facilitate physical interpretation of learned features⁶².

The second model is a modified ResNet-18 architecture pre-trained on the ImageNet dataset^{55,56}. The final classification layer is replaced by a fully connected regression head producing a single scalar output. The residual connections in ResNet-18 provide a robust feature extractor capable of capturing subtle variations in momentum-space textures, enabling comparison between task-specific and general-purpose architectures.

Both models are trained by minimizing the mean squared error loss between the predicted and true interaction strengths using Adam optimizer. Model performance is evaluated using standard regression metrics, including the mean absolute error (MAE), root-mean-square error (RMSE), and coefficient of determination R^2 . All the hyper-parameters used to train both models are listed in an appendix A.

D. Model Interpretability and Auxiliary Analyses

To verify that the neural networks base their predictions on physically meaningful FT-LDOS features rather than numerical artifacts, we apply interpretability techniques adapted to regression tasks. Gradient-weighted class activation mapping (Grad-CAM) is used to identify regions in the final convolutional layers whose activations contribute most strongly to the predicted interaction strength⁵⁷. The resulting heatmaps highlight momentum-space regions that control the regression.

Guided backpropagation is employed to obtain high-resolution saliency maps at the input level, revealing which specific pixels in the FT-LDOS images influence the output most strongly^{57,62}. Combining Grad-CAM and guided backpropagation allows simultaneous identification of relevant momentum-space regions and fine-scale spectral features.

In addition to neural-network-based analysis, we perform auxiliary dimensionality-reduction and baseline regression studies. Principal component analysis (PCA) is applied to the standardized FT-LDOS images to quantify the intrinsic dimensionality of the dataset, and a ridge regression model trained on the leading principal components provides a linear baseline for comparison with the CNN results^{38,40,41}.

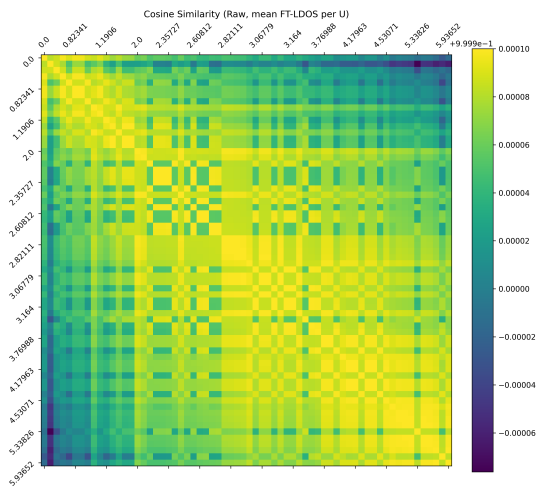


FIG. 5: **Spectral Similarity:** Cosine similarity between the FT-LDOS magnitude maps across the surveyed range of U (exceeding 99.98%)

IV. RESULTS AND DISCUSSION

Our main result is that the trained CNNs achieve highly accurate regression of the Hubbard interaction from simulated STM FT-LDOS images. In the following, we will discuss several aspects of our approach.

A. Evolution of FT-LDOS with Interaction Strength

Before discussing machine-learning performance, it is instructive to examine how the Fourier-transformed LDOS (FT-LDOS) evolves as a function of the on-site interaction U . Across the range $U = 0 - 5$ eV, the dominant features of the FT-LDOS, namely the positions of the principal moiré Bragg peaks remain unchanged, reflecting the robustness of the underlying moiré lattice geometry.

Fig. 5 shows the pairwise cosine similarity between the mean FT-LDOS images corresponding to different interaction strengths. All values lie in the range 0.9998-1.0000, indicating that the raw images are extremely similar in a global linear sense. This high similarity is expected: varying U primarily induces subtle redistributions of spectral weight rather than large structural changes in the Fourier-space LDOS. Consequently, simple distance metrics are insufficient to distinguish different U values directly. The success of the neural-network models therefore demonstrates their ability to extract weak but systematic features from high-dimensional data that are not captured by naive similarity measures.

To further analyze the intrinsic structure of the dataset, principal component analysis (PCA) was ap-

plied to the flattened FT-LDOS images. The first three principal components capture the majority of the variance, with PC1 accounting for 56.8%, PC2 for 26.8%, and PC3 for 6.1%, corresponding to a cumulative explained variance of 89.7%. This indicates that despite the high dimensionality of the images, their dominant variations lie on a relatively low-dimensional manifold. The spatial structure of the leading components, shown in Fig. 6, reveals that changes associated with U are concentrated primarily around specific momentum-space regions rather than being uniformly distributed. These observations support the suitability of learning-based approaches, as the relevant information is encoded in a small number of coherent modes rather than in high-dimensional noise.

The dominance of a small number of principal components suggests that the neural networks primarily need to learn a mapping from a compact latent representation to the interaction parameter U , explaining the high regression accuracy obtained despite the limited dataset size. Furthermore, the projection of the FT-LDOS images onto the leading principal component exhibits a nearly monotonic dependence on the interaction strength U (Fig. 7). Inspection of the corresponding eigenvector indicates that PC1 primarily encodes the contrast between the central (moiré) momentum peak and the outer graphene Bragg peaks. This behavior demonstrates that a simple, physically interpretable linear feature already carries substantial information about U , providing an intuitive baseline for understanding why the interaction strength can be inferred from STM-derived observables.

B. Regression of Interaction Strength from FT-LDOS

Model performance was evaluated over three independent random seeds (17, 42, and 101) to assess robustness against data splitting. On the standard test set containing previously seen U values, both architectures achieved consistently high accuracy. The custom CNN obtained an average test performance of MAE=0.14±0.03 eV, RMSE=0.21±0.02 eV, and $R^2=0.984±0.003$. The modified ResNet-18 model yielded comparable results with MAE=0.12±0.02 eV, RMSE=0.21±0.04 eV, and $R^2=0.985±0.006$. These results demonstrate that the mapping from FT-LDOS images to the interaction parameter U can be learned reliably when evaluated within the discrete training manifold.

To place these numbers in context, a linear ridge regression model trained on the leading PCA components attains an average $R^2 \approx 0.91$ on the same test sets. The improved performance of the CNNs therefore reflects their ability to exploit nonlinear combinations of momentum-space features beyond the dominant linear trend captured by PCA.

To assess interpolation capability, both models were additionally tested on a held-out dataset containing

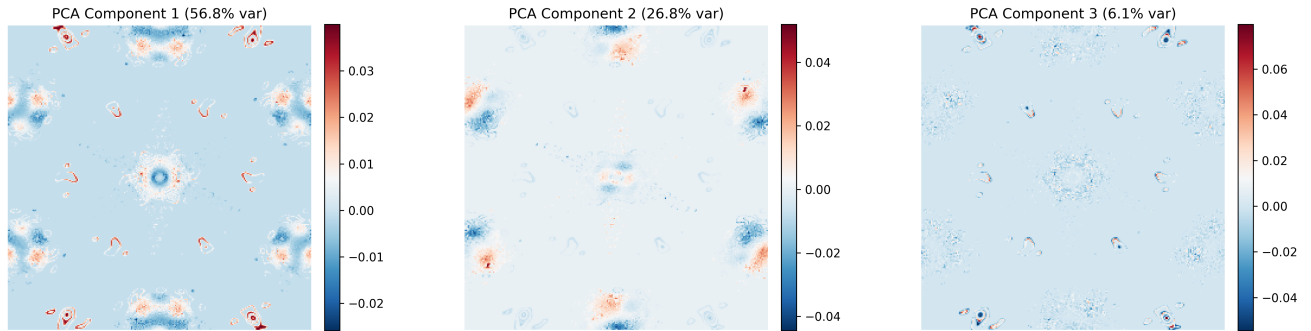


FIG. 6: Leading principal components of the FT-LDOS dataset. The top of each panel indicates the fraction of total variance explained by the corresponding component: PC1 (56.8%), PC2 (26.8%), and PC3 (6.1%). Together, the first three components capture 89.7% of the total variance, demonstrating that the dataset possesses a strongly low-dimensional structure. Color scales represent the signed amplitude of each component in momentum space (arbitrary units).

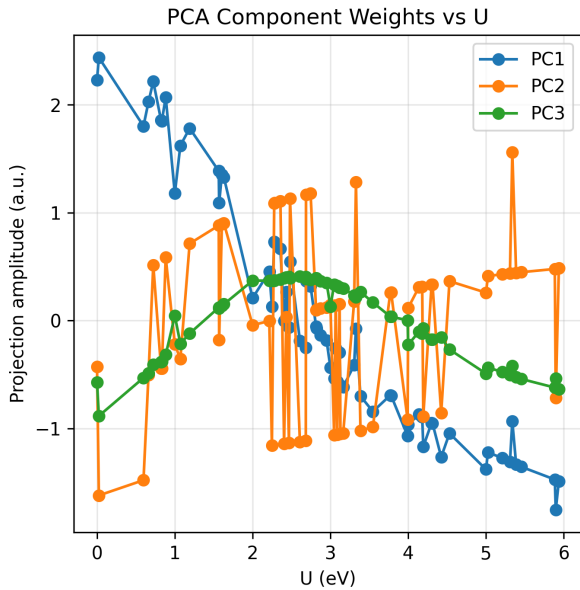


FIG. 7: Projection amplitudes of the FT-LDOS images onto the first three principal components as a function of interaction strength U . Each point represents the coefficient obtained by projecting the mean image corresponding to a given U value onto the respective PCA eigenvector. The leading component (PC1) exhibits an approximately monotonic dependence on U , indicating that a dominant linear feature of the data is directly correlated with the interaction strength. Higher components capture more subtle variations with weaker and less systematic trends.

fractional U values not encountered during training. As expected, performance decreased in this more challenging scenario. The CNN achieved $\text{MAE}=0.50\pm 0.08$ eV and $R^2=0.87\pm 0.04$, while ResNet-18 obtained $\text{MAE}=0.49\pm 0.02$ eV and $R^2=0.85\pm 0.01$. These re-

TABLE I: Performance metrics averaged over three random seeds (mean \pm standard deviation).

Model	MAE (eV)	RMSE (eV)	R^2
CNN (test)	0.14 ± 0.03	0.21 ± 0.02	0.984 ± 0.003
CNN (held-out)	0.50 ± 0.08	0.54 ± 0.07	0.87 ± 0.04
ResNet-18 (test)	0.12 ± 0.02	0.21 ± 0.04	0.985 ± 0.006
ResNet-18 (held-out)	0.49 ± 0.02	0.57 ± 0.02	0.85 ± 0.01

sults confirm that the models retain meaningful predictive power beyond the discrete grid of training parameters, although with reduced accuracy compared to in-distribution evaluation.

The reduced performance on the held-out set reflects the more challenging task of extrapolating to interaction strengths not encountered during training. This behavior indicates that while the networks successfully interpolate within the training distribution, generalization across previously unseen U values ($U \gtrsim 6$ eV) remains more difficult, resulting in the need for larger and more diverse datasets.

C. CNNs as Detectors of Interaction-Driven Spectral Redistribution

To elucidate which FT-LDOS features control the regression, we apply interpretability tools adapted to regression tasks. Grad-CAM visualizations (Fig. 8) reveal a systematic shift in the regions of momentum space most relevant to the predicted interaction strength. At weak coupling ($U \lesssim 1$ eV), the CNNs attend broadly to both central and satellite moiré peaks. As the interaction increases to intermediate values ($U \approx 2 - 3$ eV), attention becomes increasingly focused on the relative intensity contrast between these features. In the strong-coupling regime ($U \gtrsim 4$ eV), the response localizes predominantly near the Γ -point region.

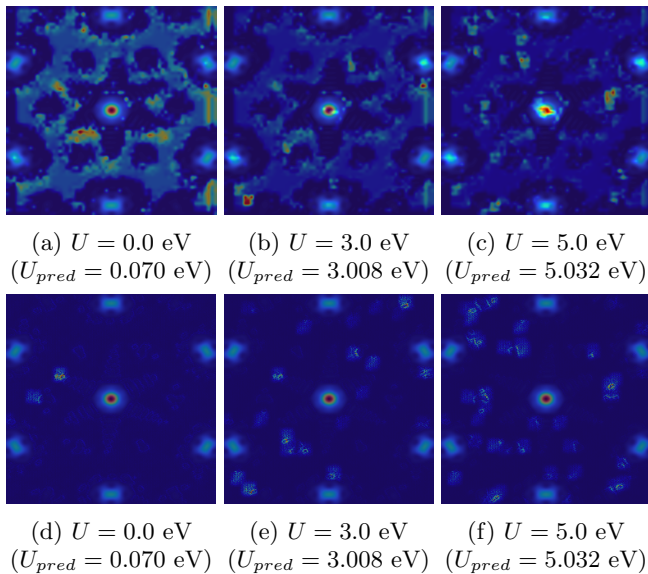


FIG. 8: Momentum-space interpretability of the custom CNN regressor for representative interaction strengths U . **Top row:** Grad-CAM visualizations showing the transition from wide-angle lattice weighting ($U = 0.0$) to hyper-localized core focus ($U = 5.0$). **Bottom row:** Guided Backpropagation resolves the pixel-level saliency within the reciprocal lattice peaks. Predicted values (U_p) are provided in parentheses for each case.

Guided backpropagation further resolves these trends at the pixel level. Saliency maps indicate that the CNNs respond primarily to sharp gradients at the edges of reciprocal lattice peaks rather than to diffuse background regions, confirming sensitivity to interaction-induced changes in peak width and relative spectral weight. Regions of stochastic background contribute negligibly to the regression signal.

D. Crossover between weak and strong Hubbard interaction

As already mentioned, Grad-CAM visualizations and guided backpropagation suggest that there is a crossover between the weak and strong Hubbard interaction regime around $U \sim t = 2.7\text{eV}$. Also from the principal component analysis, we can draw this conclusion. In Fig. 7, one sees that PC1 as function of U is monotonically decreasing with a zero at $U \sim t = 2.7\text{eV}$. PC2 is more fluctuating and can be decomposed in three main branches, all monotonically increasing and the middle one with a zero again at $U \sim t = 2.7\text{eV}$. Finally, PC3 displays a maximum at $U \sim t = 2.7\text{eV}$.

The atomistic Hubbard interaction has important im-

plications for the emergence of magnetic phases in correlated systems. For single-layer graphene at half filling, antiferromagnetism is stable beyond a critical Hubbard interaction $U_c/t \sim 2.23$.^{63,64} For twisted bilayer graphene at the magic angle, this critical value is considerably reduced and estimated to be $U_c/r \sim 0.23$,⁶⁵ consistent with the approach of 66 and still sufficient to induce ferromagnetism.⁶⁷ One of our conclusions of this work is that even for unpolarized electronic states, there might be some crossover at a critical on-site interaction strength $U_c/r \sim 1$.

V. SUMMARY

We have implemented a CNN for image recognition of STM-data. Our results demonstrate that FT-LDOS images obtained from realistic Hartree-Fock modelling can be used to quantitatively infer effective interaction strengths in correlated moiré materials. The above discussion also shows that the CNNs effectively act as electronic cross-over detectors, achieving high prediction accuracy (with coefficients of determination $R^2 \gtrsim 0.95$ on test data) and robust interpolation for fractional U values near the critical regime, where the dominant FT-LDOS weight shifts from central moiré peaks to satellite ordering vectors.^{47,48} This establishes a practical route to inferring effective interaction strengths directly from STM data in correlated moiré materials, and paves the way for combined theory ML-STM frameworks to quantify microscopic parameters in future experiments on twisted multilayers and related systems.

We believe that methodology is readily transferable to experimental STM data on twisted bilayers and multilayers, and can be extended to other parameters such as screening length, strain, or twist-angle inhomogeneity, providing a powerful, data-driven route to Hamiltonian learning in quantum materials.

DATA AVAILABILITY

All code used for dataset generation, model training, evaluation, and analysis is openly available in Zenodo at <https://doi.org/10.5281/zenodo.18717017>. The source code is also maintained on GitHub at <https://github.com/nachiket273/tbg-stm-ftldos-hubbard-U-regression>.

Acknowledgement. The work was supported by grant PID2023-146461NB-I00 funded by MCIN/AEI/10.13039/501100011033 as well as by the CSIC Research Platform on Quantum Technologies PTI-001. The access to computational resources of CESGA (Centro de Supercomputación de Galicia) is also gratefully acknowledged.

- ¹ Y. Cao, V. Fatemi, S. Fang, K. Watanabe, T. Taniguchi, E. Kaxiras, and P. Jarillo-Herrero, *Nature* **556**, 43 (2018).
- ² M. Yankowitz, S. Chen, H. Polshyn, Y. Zhang, K. Watanabe, T. Taniguchi, D. Graf, A. F. Young, and C. R. Dean, *Science* **363**, 1059 (2019).
- ³ S. Moriyama, Y. Morita, K. Komatsu, K. Endo, T. Iwasaki, S. Nakaharai, Y. Noguchi, Y. Wakayama, E. Watanabe, D. Tsuya, K. Watanabe, and T. Taniguchi, "Observation of superconductivity in twisted bilayer graphene," (2019), arXiv:1901.09356.
- ⁴ E. Codecido, Q. Wang, R. Koester, S. Che, H. Tian, R. Lv, S. Tran, K. Watanabe, T. Taniguchi, F. Zhang, M. Bockrath, and C. N. Lau, *Sci. Adv.* **5**, eaaw9770 (2019).
- ⁵ C. Shen, N. Li, S. Wang, Y. Zhao, J. Tang, J. Liu, J. Tian, Y. Chu, K. Watanabe, T. Taniguchi, R. Yang, Z. Y. Meng, D. Shi, and G. Zhang, "Correlated states in twisted double bilayer graphene," (2019), arXiv:1903.06952.
- ⁶ X. Lu, P. Stepanov, W. Yang, M. Xie, M. A. Aamir, I. Das, C. Urgell, K. Watanabe, T. Taniguchi, G. Zhang, A. Bachtold, A. H. MacDonald, and D. K. Efetov, *Nature* **574**, 653 (2019).
- ⁷ G. Chen, A. L. Sharpe, P. Gallagher, I. T. Rosen, E. J. Fox, L. Jiang, B. Lyu, H. Li, K. Watanabe, T. Taniguchi, J. Jung, Z. Shi, D. Goldhaber-Gordon, Y. Zhang, and F. Wang, *Nature* **572**, 215 (2019).
- ⁸ C. Xu and L. Balents, *Phys. Rev. Lett.* **121**, 087001 (2018).
- ⁹ H. Guo, X. Zhu, S. Feng, and R. T. Scalettar, *Phys. Rev. B* **97**, 235453 (2018).
- ¹⁰ J. F. Dodaro, S. A. Kivelson, Y. Schattner, X. Q. Sun, and C. Wang, *Phys. Rev. B* **98**, 075154 (2018).
- ¹¹ G. Baskaran, "Theory of emergent superconductivity in magic angle graphene superlattices," (2018), arXiv:1804.00627.
- ¹² Y. Cao, D. Chowdhury, D. Rodan-Legrain, O. Rubies-Bigorda, K. Watanabe, T. Taniguchi, T. Senthil, and P. Jarillo-Herrero, *Phys. Rev. Lett.* **124**, 076801 (2020).
- ¹³ M. Koshino, N. F. Q. Yuan, T. Koretsune, M. Ochi, K. Kuroki, and L. Fu, *Phys. Rev. X* **8**, 031087 (2018).
- ¹⁴ J. Kang and O. Vafek, *Phys. Rev. X* **8**, 031088 (2018).
- ¹⁵ H. Isobe, N. F. Q. Yuan, and L. Fu, *Phys. Rev. X* **8**, 041041 (2018).
- ¹⁶ L. Zou, H. C. Po, A. Vishwanath, and T. Senthil, *Phys. Rev. B* **98**, 085435 (2018).
- ¹⁷ T. J. Peltonen, R. Ojajärvi, and T. T. Heikkilä, *Phys. Rev. B* **98**, 220504 (2018).
- ¹⁸ D. M. Kennes, J. Lischner, and C. Karrasch, *Phys. Rev. B* **98**, 241407 (2018).
- ¹⁹ F. Guinea and N. R. Walet, *Proc. Natl. Acad. Sci. USA* **115**, 13174 (2018).
- ²⁰ J. González and T. Stauber, *Phys. Rev. Lett.* **122**, 026801 (2019).
- ²¹ A. Thomson, S. Chatterjee, S. Sachdev, and M. S. Scheurer, *Phys. Rev. B* **98**, 075109 (2018).
- ²² S. Carr, S. Fang, P. Jarillo-Herrero, and E. Kaxiras, *Phys. Rev. B* **98**, 085144 (2018).
- ²³ D. Călugăru, Y. Jiang, H. Hu, H. Pi, J. Yu, M. G. Vergniory, J. Shan, C. Felser, L. M. Schoop, D. K. Efetov, K. F. Mak, and B. A. Bernevig, *Nature* **643**, 376 (2025).
- ²⁴ C.-C. Liu, L.-D. Zhang, W.-Q. Chen, and F. Yang, *Phys. Rev. Lett.* **121**, 217001 (2018).
- ²⁵ Y.-Z. You and A. Vishwanath, *npj Quantum Materials* **4**, 16 (2019).
- ²⁶ Y.-H. Zhang, D. Mao, Y. Cao, P. Jarillo-Herrero, and T. Senthil, *Phys. Rev. B* **99**, 075127 (2019).
- ²⁷ J. González and T. Stauber, *Phys. Rev. Lett.* **124**, 186801 (2020).
- ²⁸ K. P. Nuckolls *et al.*, *Nature* **620**, 525 (2023).
- ²⁹ H. Kim *et al.*, *Nature* **623**, 942 (2023).
- ³⁰ D. Calugaru *et al.*, *Physical Review Letters* **129**, 117602 (2022).
- ³¹ Y. H. Kwan *et al.*, arXiv preprint (2023), 2303.13602.
- ³² Y. Choi, J. Kemmer, Y. Peng, A. Thomson, H. Arora, R. Polski, Y. Zhang, H. Ren, J. Alicea, G. Refael, F. von Oppen, K. Watanabe, T. Taniguchi, and S. Nadj-Perge, *Nature Physics* **15**, 1174 (2019).
- ³³ Y. Xie, B. Lian, B. J"ack, X. Liu, C.-L. Chiu, K. Watanabe, T. Taniguchi, B. A. Bernevig, and A. Yazdani, *Nature* **572**, 101 (2019).
- ³⁴ J. Mao, S. P. Milovanovi'c, M. Andelkovi'c, X. Lai, Y. Cao, K. Watanabe, T. Taniguchi, L. Covaci, F. M. Peeters, A. K. Geim, Y. Jiang, and E. Y. Andrei, *Nature* **584**, 215 (2020).
- ³⁵ Y. Choi, H. Kim, C. Lewandowski, Y. Peng, A. Thomson, R. Polski, Y. Zhang, K. Watanabe, T. Taniguchi, J. Alicea, and S. Nadj-Perge, *Nature Physics* **17**, 1375 (2021).
- ³⁶ K. P. Nuckolls, R. L. Lee, M. Oh, D. Wong, T. Soejima, J. P. Hong, D. Călugăru, J. Herzog-Arbeitman, B. A. Bernevig, K. Watanabe, T. Taniguchi, N. Regnault, M. P. Zaletel, and A. Yazdani, *Nature* **620**, 525 (2023).
- ³⁷ X. Lai, G. Li, A. M. Coe, J. H. Pixley, K. Watanabe, T. Taniguchi, and E. Y. Andrei, *Nature Materials* **24**, 1019 (2025).
- ³⁸ G. Carleo *et al.*, *Reviews of Modern Physics* **91**, 045002 (2019).
- ³⁹ A. Dawid *et al.*, arXiv preprint (2022), 2204.04198.
- ⁴⁰ E. Chertkov and B. K. Clark, *Physical Review X* **8**, 031029 (2018).
- ⁴¹ A. Dubois *et al.*, *Physical Review Applied* **18**, 064076 (2022).
- ⁴² K. Choudhary *et al.*, *Scientific Data* **8**, 57 (2021).
- ⁴³ F. Joucken *et al.*, *Physical Review Materials* **6**, 123802 (2022).
- ⁴⁴ J. Liu, D. Huang, Y. F. Yang, and T. Qian, *Physical Review B* **107**, 165106 (2023).
- ⁴⁵ J. F. Rodriguez-Nieva and M. S. Scheurer, *Nature Physics* **15**, 790 (2019).
- ⁴⁶ M. S. Scheurer and R.-J. Slager, *Physical Review Letters* **124**, 226401 (2020).
- ⁴⁷ J. A. Sobral, S. Obernauer, S. Turkel, A. N. Pasupathy, and M. S. Scheurer, *Nature Communications* **14** (2023), 10.1038/s41467-023-40684-1.
- ⁴⁸ W. Taranto, S. Lederer, Y. Choi, P. Izmailov, A. G. Wilson, S. Nadj-Perge, and E.-A. Kim, arXiv preprint (2022), arXiv:2203.04449 [cond-mat.str-el].
- ⁴⁹ M. Sánchez Sánchez, I. Díaz, J. González, and T. Stauber, *Physical Review Letters* **133**, 266603 (2024).
- ⁵⁰ M. Sánchez Sánchez, J. González, and T. Stauber, *Physical Review B* **111**, 205133 (2025).
- ⁵¹ P. Moon and M. Koshino, *Phys. Rev. B* **87**, 205404 (2013).
- ⁵² R. E. Throckmorton and O. Vafek, *Phys. Rev. B* **86**, 115447 (2012).

- ⁵³ Y. Saito, J. Ge, K. Watanabe, T. Taniguchi, and A. F. Young, *Nature Physics* **16**, 926 (2020).
- ⁵⁴ P. Stepanov, I. Das, X. Lu, A. Fahimniya, K. Watanabe, T. Taniguchi, F. H. L. Koppens, J. Lischner, L. Levitov, and D. K. Efetov, *Nature* **583**, 375 (2020).
- ⁵⁵ K. He, X. Zhang, S. Ren, and J. Sun, “Deep residual learning for image recognition,” (2015), arXiv:1512.03385 [cs.CV].
- ⁵⁶ O. Russakovsky, J. Deng, H. Su, J. Krause, S. Satheesh, S. Ma, Z. Huang, A. Karpathy, A. Khosla, M. Bernstein, A. C. Berg, and L. Fei-Fei, *International Journal of Computer Vision (IJCV)* **115**, 211 (2015).
- ⁵⁷ J. Gildenblat and contributors, “Pytorch library for cam methods,” <https://github.com/jacobgil/pytorch-grad-cam> (2021).
- ⁵⁸ M. Sánchez Sánchez, J. González, and T. Stauber, *Phys. Rev. B* **111**, 205133 (2025).
- ⁵⁹ T. Stauber, M. Sánchez Sánchez, I. Vasilevskiy, J. González, J. C. Mouriño Gallego, M. Wackerl, P. Wenk, and J. Schliemann, “Forge: Fock optimization of real-space giant environment,” (2025).
- ⁶⁰ G. Trambly de Laissardière, D. Mayou, and L. Magaud, *Nano Letters* **10**, 804 (2010).
- ⁶¹ M. S. Sánchez and T. Stauber, *Phys. Rev. B* **113**, 035155 (2026).
- ⁶² I. J. Goodfellow, J. Shlens, and C. Szegedy, arXiv preprint (2014), arXiv:1412.6572 [stat.ML].
- ⁶³ S. Sorella and E. Tosatti, *Europhysics Letters* **19**, 699 (1992).
- ⁶⁴ F. F. Assaad and I. F. Herbut, *Phys. Rev. X* **3**, 031010 (2013).
- ⁶⁵ J. Vahedi, R. Peters, A. Missaoui, A. Honecker, and G. T. de Laissardière, *SciPost Phys.* **11**, 083 (2021).
- ⁶⁶ J. González and T. Stauber, *Phys. Rev. B* **102**, 081118 (2020).
- ⁶⁷ R. Pons, A. Mielke, and T. Stauber, *Phys. Rev. B* **102**, 235101 (2020).

Appendix A: Training Hyper-Parameters

This appendix summarizes the hyper-parameter values used for all neural-network models reported in the main text. The values listed here were fixed across all training runs and random data splits unless stated otherwise.

All convolutional neural networks were trained using the Adam optimizer. The initial learning rate was set to 10^{-4} for the custom CNN and to 10^{-3} for the modified ResNet-18 architecture. The optimizer momentum parameters were $\beta_1 = 0.9$ and $\beta_2 = 0.999$. A cosine annealing learning-rate schedule was employed, with a minimum learning rate of 10^{-6} . The batch size was fixed at 32 for all experiments.

Models were trained for a maximum of 40 epochs, with early stopping based on the validation loss using a patience of 10 epochs. A weight decay of 10^{-4} was applied to mitigate overfitting. No data augmentation was used for the FT-LDOS images. To ensure numerical stability during training, gradient clipping with a maximum norm of 1.0 was applied.

The mean squared error between the predicted and target interaction strengths was used as the training loss. Model performance was evaluated using the mean absolute error (MAE), root-mean-square error (RMSE), and the coefficient of determination R^2 , as reported in Table I. All reported results correspond to the same hyper-parameter configuration across different random training-test splits.

Training was performed using fixed random seeds (17, 42, and 101) to ensure reproducibility. The full implementation, including configuration files specifying all hyper-parameters and random seeds, will be made publicly available upon publication.